

## Research Article

# Reconstructing the Photoacoustic Image with High Quality using the Deep Neural Network Model

Anitha Gopalan,<sup>1</sup> O. Vignesh,<sup>2</sup> R. Anusuya,<sup>3</sup> K. P. Senthilkumar,<sup>2</sup> V. S. Nishok,<sup>4</sup> T. Helan Vidhya,<sup>5</sup> and Florin Wilfred <sup>6</sup>

<sup>1</sup>Department of Electronics and Communication Engineering, Saveetha School of Engineering, SIMATS, Chennai 602 105, Tamil Nadu, India

<sup>2</sup>Department of Electronics and Communication Engineering, Easwari Engineering College, Ramapuram, Chennai, Tamil Nadu, India

<sup>3</sup>Department of Computer Science and Engineering, Modern Institute of Technology and Research Centre, Alwar, Rajasthan, India

<sup>4</sup>Department of Electronics and Communication Engineering, QIS College of Engineering and Technology, Ongole, Andhra Pradesh, India

<sup>5</sup>Department of Electronics and Communication Engineering, Rajalakshmi Engineering College, Chennai, Tamil Nadu, India

<sup>6</sup>Department of Electrical, Electronics and Communication Engineering, St. Joseph College of Engineering and Technology, St. Joseph University in Tanzania, Dar es Salaam, Tanzania

Correspondence should be addressed to Florin Wilfred; [florin.wilfred@sjuit.ac.tz](mailto:florin.wilfred@sjuit.ac.tz)

Received 25 August 2022; Revised 29 September 2022; Accepted 11 October 2022; Published 15 May 2023

Academic Editor: Yuvaraja Teekaraman

Copyright © 2023 Anitha Gopalan et al. This is an open access article distributed under the Creative Commons Attribution License, which permits unrestricted use, distribution, and reproduction in any medium, provided the original work is properly cited.

The range of diagnostic equipment has been widened and improved by the quick development of biomedical research technologies. The creation of multifunctional instruments that become essential for biomedical operations has been discovered by several research organizations to be made possible by optical imaging, acoustic image analysis, and magnetic resonance imaging. One of the most crucial tools is hyperspectral photoacoustic (PA) imaging, which combines optical and ultrasonic technology. In this study, the reconstruction of the PA pictures employs a new deployment of deep learning methods. This enabled us to train and evaluate our deep-learning approach under several imaging situations in addition to firmly establishing the contextual information. This study presents an optimization approach that blends multispectral optical acoustic imaging with detailed transfer learning-based diagnostic imaging. The particle swarm-convolutional neural network (PS-CNN) technique aims to reconstruct and categorize the presence of cancer using ultrasonic pictures. In image processing, the technique of bilateral filtration (BF) is commonly employed to remove noise. Additionally, the biological images are separated using portable LED Net frameworks. It is also possible to employ a feature extraction technique with the PS optimization methodology. Last but not least, biological images employ a CNN model to assign suitable classification. Using a standard dataset, the PS-CNN technology's efficacy is confirmed, and testing findings revealed that it performs superior to other methods.

## 1. Introduction

A nonionizing, noninvasive multimodal imaging approach called photoacoustic (PA) imaging has developed greatly over time to the extent where clinical studies are now a real possibility. Owing to its flexible nature, which combines optical stimulation and acoustic recognizing, photoacoustic imaging (PAI) benefits from both great (diffraction limited) positioning precision in relation to the propagation of low-scattering ultrasonic

waves. PA photography overcomes the scattering constraint of high visual imaging by utilizing electromagnetic energy-caused ultrasonic vibrations as a conveyance to capture absorption spectrum characteristics of tissues. Its ability to effectively realize the architectural or operational aspects of cellular structures makes PAI, a relatively new imaging methodology, a powerful tool for studying the physiological, pathological, morphological, and metabolism aspects of biological matter. The PA effect is

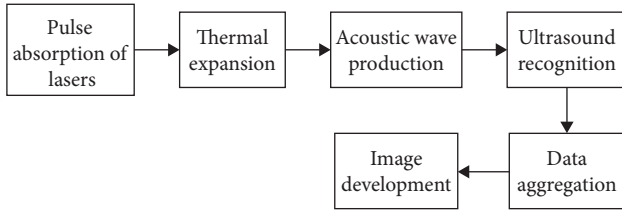


FIGURE 1: Workflow of photoacoustic imaging.

evident when visually sensitive cells are exposed to short nano-second pulse lasers. When the goal fascinates the pulsation energy with the aid of heat, a transitory temperatures rise and a regional enhancement in pressure waves due to thermoelasticity compression occur [1].

A novel hybrid imaging technique that combines both optical and ultrasonic intensity is called PAI. Because optical imaging has the ability to distinguish between hypoxic blood pools, it has been demonstrated to find and describe a range of vascular anomalies in the breast. In order to identify several vascular irregularities currently discovered by MRI scans, with gadolinium-based comparison composite infusions and expensive demand and complexity, PAI could possibly add substantially to static or dynamic distinction research, trying to seek for vascular diseases and breast preventative care. The use of PAI for breast cancer detection has been covered in a number of studies. When using a microwave to generate thermoacoustic imaging, the amount of ionized fluid in the breast cells responded. Moreover, the business uses PAI at a reasonably high frequency of 5 MHz and significant focused amplification of microscopic ultrasound (US) components on a rotating disc to perform an astonishingly thorough chest angiography on a single person. Researchers created 20 approaches for 3D screening mammography that utilize a planar 2D matrix with 590 elements carried out by a unified processing flow [2].

A key component of PAI image analysis, which is a brand-new hybrid imaging technique that merges visual stimulation of the targeted respondents with acoustic recognition produced by the sample's temperature expansion, as shown in Figure 1, is photoacoustic computational tomography (PACT). PACT generates PA energy by diffusing high-intensity pulsing laser beam to cover the specimen tissues in a complete area irradiation [3]. Wideband ultrasonic transducers are utilized to gather the frequencies near the tissues. A data collecting unit is utilized to gather the ultrasonic waves from the item, and an image reconstruction algorithm is then employed to rebuild a PACT images. The image depicts the tissue's vascular and functional data. The creation of imaging technologies as a consequence of increasing R&D investments and the rapid speed of technology innovations is what is largely fueling the expansion of the worldwide experimental imaging market [4]. By the conclusion of 2018, it is predicted that the worldwide high-resolution image processing market will reach over \$1.9 billion, increasing at an 11.37%. PA and near-infrared spectroscopic together provide around 6.85% of all visual imaging techniques [5]. For deep tissue mapping at a distance of a few centimeters, PACT developed favorably when the poor quality was adequate

[6]. This approach has been used in a number of clinical and preclinical activities over the last several decades, involving functioning brain imaging, small-animal whole-body imaging, breast cancer screening, and lymphatic nodes surgical guiding [7]. PACT has undergone several upgrades to address its drawbacks [8]. Because acoustic dispersion in tissues is around three times of magnitude less than visual dispersion, PAI is more prominent than visual imaging techniques [9]. The particle swarm (PS) and convolutional neural network (CNN) approach's individual modules are described in-depth in the subsequent sections.

## 2. Related Works

Due to its potential to move from a lab setting to a clinical one, photoacoustic tomography (PAT) restoration is rapidly gaining attention across biomedical researchers. However, under real limits, the PAT inversion issue has not yet found an ideal solution for quick and accurate reconstructions. The key challenges to achieving accurateness are, specifically, the sparse sampling issue and random noise, which facilitate quick PAT restoration. The constraints stem from the acquisition of under-sampled artifacts, which reduce the effectiveness of the restoration effort. Consequently, the modality is restricted to clinical contexts by earlier successes in quick image generation. Therefore, the study investigates a deep learning-based generative adversarial network (GAN) to denoise and eliminate these artifacts, hence enhancing the quality of the image. The primary driving force behind the use of GAN is it's specifically created properties and distinctive approach to problem optimization, which incorporates dataset constraints and offers steady performance of the model. Additionally, using the *U-Net* variation as a generator network provides strong results in terms of quality and computational price, which is further supported by the in-depth both quantitative and qualitative study. The result of the study indicates that the suggested approach generates a high-resolution image even after learning with a low-quality set of data. This approach is not efficient because massive amount of data is required for the training phase and also needs high computation power [10].

In diverse clinical diagnostics, including cancer detection, vascular imaging, and surgical navigation, PAI technology is beneficial. The received RF signals are made up of the direct-arrived signals from the PA sources and the boundary-reflected signals (BRS), despite the fact that the majority of imaging objects are bounded. During the process of reconstructing the image, the unwanted BRS will significantly decrease the quality. It will bring in a lot of artifacts, which will obscure the true nature and positioning of the PA sources. By deleting the BRS before the standard redevelopment process in order to suppress such artifacts, the reconstructing procedure was made better. The research contrasted the experimental outcomes of the conventional and improved processes in order to validate the suggested strategy. The enhanced procedure's rebuilt images show less artifacts and more precise forms of the PA sources when it comes to

qualitative inspection. The distributed relative error (DRE) among each results of the experiment and its standardized design of the phantoms was determined in order to objectively compare the conventional and the improved imaging methods. The DREs of rebuilding produced by the improved reconstruction process dramatically reduce for both phantoms and the ex vivo material. The findings imply that the optimized reconstruction method may successfully reduce reflection artifacts and enhance the PA sources' form precision [11].

In order to greatly increase the quality and SNR of the out-of-focus sector, this work proposes a new PA/US endoscopy image reconstruction technique depending on the approximately Gaussian acoustic field. For used numerical simulations to illustrate the process, and study looked at how well the program worked using a chicken breast phantom. The rabbit rectal endoscopy test was the last step in the testing procedure. According to simulated findings, this innovative method can effectively maximize the resolution of the target position in the out-of-focus area. The lateral resolution of the indocyanine green (ICG) tube in the PA image is lowered from 4 to 2 mm by utilizing the novel technique that is a 52% enhancement, according to findings from phantom experiments. The lateral resolution of US images has significantly improved as well. The findings of the rabbit rectal endoscopy test demonstrate the superior PA/US image resolution of the method suggested. As a result, the algorithm substantially enhances the image usability of the system and allows quick acoustic resolutions PA/ultrasonic dynamic focusing, providing important direction for the construction of acoustic resolutions PA/US endoscopic technologies [12].

With the precise detection of critical tissue locations and invasive clinical equipment, PAI has demonstrated significant promise for directing minimally invasive operations (such as metallic needles). Due to their great mobility and affordability, light-emitting diodes (LEDs) are increasingly being used in therapeutic settings. Furthermore, the low optical fluence of LED-based PAI compromises needle accessibility. In order to increase the appearance of medical metallic needles with an LED-based PA and ultrasonic imaging system, this research proposed a deep-learning platform based on *U-Net*. This structure included the advancement of semisynthetic training sets incorporating both synthetic data to demonstrate characteristics from the needles and in vivo evaluation for tissue surroundings in addition to addressing the challenge of obtaining true data for actual data as well as the poor realism of mainly simulation data. Assessments on human volunteers, ex vivo tissues from pork joints, and needle substitutions into blood vessel-imitating phantoms were used to evaluate the learned neural network. By repressing background noise and image artifacts, this deep learning-based structure significantly increased the needle accessibility in PAI in vivo when compared to conventional rebuilding, accomplishing 5.8 and 4.5 times enhancement in terms of the signal-to-noise ratio and the altered Hausdorff distance, accordingly. In order to accurately identify medical needles in PAI and hence minimize difficulties during percutaneous needle injection, the

conceptual approach may be useful. In this technique, the computation time is high because the learning process is slowed down [13].

Clinical ultrasonography can be transformed by PAI by adding molecular data. Furthermore, because of the constrained angle of view and image intensity, clinical translation of PAI is still difficult. Therefore, a novel, powerful method known as Superiorized Photo-Acoustic Non-NEgative Reconstruction (SPANNER) is developed. It is intended to rebuild PA images in real-time and resolve the artifacts caused by constrained observing ranges and image intensity. The technique employs accurate forward modeling of the PA propagating and signal receptions while taking into consideration the impacts of acoustical absorbance, element size, form, and sensitivities, as well as the impulse response and directivity pattern of the transducer. For inversion, a quick superiorized conjugate gradient technique is employed. The restoration techniques delay-and-sum (DAS), universal back-projection (UBP), and model-based restoration (MBR) are contrasted with SPANNER. Combined simulated and empirical studies from tissue-imitating phantoms, ex vivo tissue samples, and in vivo prostate images of patients are used to apply all four algorithms. Simulation and phantom tests demonstrate SPANNER's capacity to raise contrasting to ambient ratio by up to 20 dB in comparison to all other techniques and to achieve axial resolution that is three times higher than that of DAS and UBP. Other three image reconstruction techniques did not produce a statistically significant change between prior and subsequent contrast agent administering when SPANNER was applied to contrast-enhanced PA images obtained from cancer patients, addressing SPANNER's effectiveness in separating intrinsic from extrinsic PA signals and its capacity to more precisely measure PA signals from the contrast medium [14].

The effectiveness of an acoustic lens-based reconstructing approach and a traditional back projected algorithm-based reconstructing approach for PAI are compared in this research. By using an acoustic lens to generate an image of the PA origin on the US transmitter array, the acoustic lens-based rebuilding method taken into consideration in this study was capable of generating 2D reconfigured images that accurately represented the objects cross-sectional planes in actual time. With the use of this method, fewer observations may be needed than would otherwise be necessary when utilizing a traditional algorithm-based reconstructing strategy. This hardware reconstructing method does not necessitate the high computational and memory demands of algorithm-based PA image restorations. This study employed a straight or a flat US transducer array to collect information from a spherical or cylindrical source. In order to assess the effectiveness of every restoration approach, three concepts utilized: full width half maximum (FWHM), Pearson correlation (PC), and energy (E). The research's findings demonstrated that the acoustic lens-based restoration method can successfully recreate 2D PA images with characteristics on par with those of algorithm-based methods [15].

The capacity of combining ultrasonic and photoacoustic (USPA) imaging to concurrently show structural, operational, and molecular data of the deepest biological tissue

in actual time has drawn interest from both preclinical and medical applications. Moreover, the USPA image capability in deep tissue areas is constrained by depth- and wavelength-dependent optical attenuation as well as unidentified optical and acoustical heterogeneities. In order to get around these restrictions and enhance the quality of the USPA images, new equipment, image restoration, and artificial intelligence (AI) techniques are now being researched. A trustworthy USPA simulation model that can provide anatomy and molecular distinctions of depth biological tissue depending on the US and PA standards is necessary for the application of these techniques to be successful. Therefore the study created a hybrid USPA simulation tool by combining light (NIRFast) and US ( $k$ -wave) propagating finite element systems for simultaneous modeling of B-mode US and PA images. The aperture dimension and wavelength of lighting and ultrasonic detection panels, as well as other design considerations for USPA systems, may all be optimized using the framework. A dictionary-based tool has been introduced to  $k$ -Wave to produce different degrees of ultrasonic speckle contrast for constructing tissue-realistic digital phantoms. Utilizing heterogeneous and homogeneous tissues phantoms that mirror real organs, the viability of modeling US images in conjunction with optical fluency-dependent multispectral PAI is established. The study also shows how the simulation tool can provide sizable testing and training datasets adapted to specific purposes for USPA imaging with AI. In conclusion, the USPA simulation tool that has been shown offers a strong tool for enhancing the functionality of dual-modality USPA imaging devices for a variety of preclinical and medical fields [16].

PA image reconstruction has gotten a lot of interest lately. There are several restoration techniques that have been established, including back-projection, frequency domain reconstruction, time reversal, and model-based restorations. Whenever rebuilding images on homogeneous media, these techniques have implements that are reasonably straightforward despite being dependent on various propagating concepts. The rebuilding procedure is complicated when heterogeneous-layered media are present, such as in PA transcranial imaging, since the propagation models must be altered to account for different acoustic impact at interface layer. In this paper, the study provides a premigration method expansion to first transform the restoration issues that concern homogenous medium. The origins can then be recreated once again utilizing conventional reconstruction techniques. Classical restorations do not need to be altered to account for premigration. It solely uses wave extrapolating to preadjust the sensor location. It also makes a concentrated transducer approach into a sensor that resembles a spot. Premigration may be included into virtually all traditional reconstruction methods and effectively resolves restoration issues when imaging via heterogeneous medium, according to simulated and experimental data. In this study, it only consumes around 20% of the overall processing time for rebuilding. The sustainable propagation angle in this method is insufficient [17].

In the past 10 years, there has been an increase in interest in the use of acoustic-resolution photoacoustic microscopy (ARPAM) for medical purposes. Synthetic aperture focusing technique (SAFT) approaches that contain the virtualized

detection (VD) idea are utilized to rebuild the pictures in order to remove the distortion brought on by acoustical diffraction in ARPAM. Furthermore, while the majority of these systems work best with homogenous media, they struggle with heterogeneous media situations. Upon this basis, the study provides an ARPAM reconstruction method that is adaptable to situations involving layered heterogeneous media. Utilizing virtualized scan plane concept, this technique reconstructs a VD-based reception system. Then, using the suggested phase-shift factors for various multilayered media, it extrapolates wave domains. Then, in order to rebuild images, it uses a nonuniform rapid Fourier transform. The calculation for multilayer material is made simpler by the waveform extrapolation, which removes refraction-related distortions. The suggested technique may rebuild high-quality images for layered heterogeneity material, as per simulations. The reliability of the system is low compared to other techniques [18].

The study provides a method for denoising PA signals that combines low-pass filtering and sparse coding (LPFSC). The LPFSC approach relies on the fact that the PA signal may be represented as the summation of lower frequencies and sparse elements, which enables the decreased levels of noise when utilizing a hybrid alternating directions multiplier method during an optimization problem. Utilizing in silico and empirical phantoms, the LPFSC approach was assessed. The maximum SNR of the PA signal has been improved by 26% as compared to the in silico information averaged approach, according to the outcomes. Considering objects positioned at three various levels, varying from 10 to 20 mm, in a porcine tissues phantom, the LPFSC approach, on median, provides a 63% enhancement in the imaging contrast-to-noise ratios and a 33% enhancement in the conceptual similarity measure comparing to the averaging method. The suggested approach is a helpful technique for PA signal denoising, and while slowing down image acquisitions, it eventually improves the appearance of image reconstruction, particularly at greater levels. In this technique stability is maintained in the filter which causes the effectiveness of the system [19].

### 3. Photoacoustic Imaging

*3.1. PA Fundamental Physics.* Researchers simply provide a cursory explanation of PAI in this article because the basics have been covered extensively in other books. A nanosecond pulsing laser beam is utilized in PAI to generate wideband PA impulses, which are detected by a number of transducers [20]. The following is an expression for the preliminary PA compression:

$$A^0 = L^0 \alpha^{th} \delta^0 P, \quad (1)$$

where  $L^0$  stands for the tissue's Gruneisen parameter,  $n^{th}$  for the efficiency of turning light into heat, for the optical absorption coefficient, and  $P$  for the local optical fluence. After the creation of  $A^0$ , the PA wave propagation in the medium can be represented by the following PA equation:



$$\left(\Delta^2 - \frac{1}{s_r^2} \frac{\partial^2}{\partial t^2}\right) A(x, y) = -\frac{\gamma}{Ts_r^2} \frac{\partial^2 K(x, y)}{\partial t^2}, \quad (2)$$

where  $T$ , the rate of warming, is the isothermal ductility, stands for the thermal coefficients of capillary forces,  $A(x, y)$  is the PA pressure at position  $r$  and time  $t$ . The heat transfer time ( $\lambda$ th) and the stress relaxation time ( $s$ ), two points of confinement in PAI, should be satisfied by the brief laser pulse duration. In particular, the laser pulse duration should be considerably shorter than  $s$  and  $\lambda$ th. The heat equation has the following form:

$$\beta I' \frac{\partial T(x, y)}{\partial t} = A(x, y). \quad (3)$$

If the aforementioned requirement is met by the laser pulse width, the resultant of the absorption spectrum coefficients and fluence ratio ( $H = \delta\beta\theta$ ) indicates the heating functionality, which is represented by the letter  $H$ . Equation (3) is substituted into Equation (2) to produce the following formula:

$$\left(\Delta^2 - \frac{1}{s_r^2} \frac{\partial^2}{\partial t^2}\right) A(x, y) = -\frac{\gamma}{T_s} \frac{\partial^2 K(x, y)}{\partial t^2}, \quad (4)$$

where the particular thermal capability at relentless pressure is indicated by the letter  $K$ .

$$A(x, y) = \frac{1}{4\pi s_r^2} \frac{\partial}{\partial t} \left[ \frac{1}{s_r t} \int dr' A^0(r') \gamma \left( t - \frac{|r - r'|}{s_r} \right) \right], \quad (5)$$

where the starting pressures at point  $r'$  is denoted by  $A^0(r')$ .

**3.2. PAI Modalities.** Some PAI methods that are quickly gaining popularity are PA microscopy and PA computed tomography. Both employ different techniques to produce visuals: the former builds a vision by examining each point in turn, while the latter reconstructs an image by assembling PA signals from several locations. Using a focused ultrasonic transducer, the tissue surface is scanned in photoacoustic microscopy (PAM). Both the visual stimulation as well as the auditory sensing are parallel in a typical PAM system. Optically resolved PAMs (OR-PAM) and acoustically resolved PAMs (AR-PAM) are two common PAMs that depending upon whether the visual emphasis or the acoustical concentrate is greater. With higher frequency transducers, OR-PAM can provide a superior resolving power from a few nanometer scale to the few micrometers in diameter. The radio bandwidth PA output experiences substantial acoustic loss, which limits the PA transmitter immersion. The circulatory morphology and label-free imaging for hemoglobin oxygen saturation can be provided by OR-PAM [21]. However, compared to the visual emphasis, the auditory priority of AR-PAM is closer. With acoustic light scattering, it obtains precision of  $10 \mu\text{m}$ . The sampling frequency and laser power resonance frequency of AR-PAM are the limiting factors for photographic velocity. Retinal blood vessels imaging on a greater scale is possible with the AR-PAM [22]. Additionally, PAM's applicability is

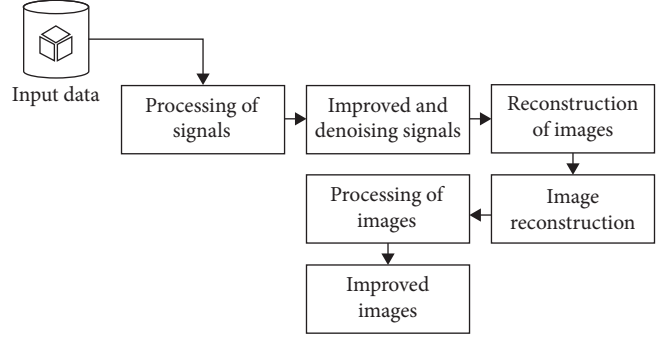


FIGURE 2: Workflow of the proposed system.

constrained by its slow scanning speed and limited scanning area. PACT uses an ultrasonic transducer array to collect PA signals from various locations, speeding up the imaging process. An extending laser light equally excites the whole region of interest (ROI), and a transducer array simultaneously detects the PA waves. Finally, a high-quality image is rebuilt utilizing reconstructing methods including time reversing and universal back-projection. It is desirable to use PACT with spatial resolution of  $100 \mu\text{m}$ , which can be enhanced by boosting the transducer array's core frequency range and bandwidth. PACT can reduce body-wide sizes [23].

## 4. Proposed Method

In this work, a novel PS- RNN method for PAI-based tumor classification and reconstruction was created. A number of processes are included in the proposed PS-CNN approach, comprising bilateral filtration depending upon preprocessing, segmentation based on LED Net, extraction of features dependent on PS, and reconstruction utilizing CNN. The PS and CNN approach's individual modules are described in this paper. The fundamental process flow for the suggested method is shown in Figure 2.

The data in Figure 2 show ultrasonic sensors beyond the tissues that detect shifts in temperature as ultrasonic vibrations. The analytics gather information on the inherent acoustical and graphical characteristics of the absorption as well as inconsistent data brought on by electromagnetic fields. In order to remove the essential PA signals from the turbulent ambient and utilize them to reconstruct a PA graphic, the acquired data is next subjected to signal conditioning analysis. These images show the inner composition and associated functioning of the tissue under study. Numerous image reconstructing approaches have been tested for PA scanning, and each of them might be viewed as a problem with the acoustic inverted sources. Conventional acoustic imaging approaches assume that the item of interest's auditory characteristics were consistent [24].

**4.1. Data Collection.** The scientific tumor findings have provided torrents website collection where the multispectral PA testing images were located. The datasets have been verified to 70:30 proportions for the preparation and evaluation of the specimens. The majority of the information is not really consistent because of the inconsistent data gathering, as well as the size of the data varied from  $20 \times 64 \times 200$  pixels to

$64 \times 64 \times 200$  pixels. By increasing the size to  $65 \times 65$  pixels and employing exclamation method, the  $X$ - and  $Y$ -directional equalization was completed.

**4.2. Data Preprocessing.** This study employs the bilateral filtration strategy as a method of image processing. It employs a nonlinear aggregation of the closure elements of the picture to give the images smoothness without altering their edges. The suggested approach is untested, basic, and localized. It blends the gray levels based on geometric closeness and optoelectronic similarity. It chooses the domains that are closest to the radius and cost range. As opposed to filtering in three independent color bands, CIELAB uses two-sided screening for essential perceptual factors in color space, preserving edges, and smoothing the color scheme [20].

**4.3. Image Segmentation.** An asymmetrical hierarchical structure is used by LED Net's encryption–decryption technique, which reduces the extracted features after encrypting and also modifies it with the APN's help to make it more suitable for the input resolution. The down-sampling method employs two parallel outputs piled on a single  $3 \times 3$  convolution with max pooling and direct two in addition to the system strain (SS)-net units. Despite reducing computing time, the down sampling offers very thorough networking to capture the circumstances. Additionally, the architecture can capture a wider acceptance area thanks to the extended convolutional process, which increases accuracy. Using a wider kernel width, this technique was created to enhance efficiency in terms of operational cost and parameters. The spatially appraisal encoded architecture APN leverages spatialwise focuses created by the attentive procedure. The APN acknowledges a pyramid focus aspect that combines the best from three different pyramid sizes to broaden the sensitive web address. It begins by combining linear two with the  $3 \times 3$ ,  $5 \times 5$ , and  $7 \times 7$  convolutions. The pyramidal design then sequentially mixes data from several aspects, seamlessly incorporating the context's adjacent aspects. Since the upper-level ROI has a smaller screen, using a bigger convolution layers does not enhance the SS. The coded impact was then subjected to a  $1 \times 1$  convolution, and the pyramid focus component created an extracted feature by multiplying pixels-by-pixels. The established worldwide mean pooled branches that incorporate the prior environment's core and improve results. The resolution of the input photos was ultimately matched using an up-sample mechanism [25].

**4.4. Extracting Features.** The segmented picture is transferred to the PS method during the extraction of characteristics to identify lesion areas in PA image analysis.

**4.5. Particle Swarm Optimization.** It is a physiologically driven mechanism that quickly determines the optimum course of action at the location of the conclusion. The procedure is initiated by choosing  $N$  random photographs. The quantity of “ $P$ ” variables that were employed to characterize the  $n$ th visual can be determined by placing it as a spot in the  $V$ -dimensional region. Throughout the “ $S$ ” phase, each picture keeps track of three pieces of information: its present location ( $P^s$ ), the maximum level attained in earlier phases

( $O^p$ ), and its flight speed ( $f^k$ ). The following are the values for these three tiers:

$$\text{Present position } P^s = P^{s1}, P^{s2}, P^{s3}, \dots, P^{sn}, \quad (6)$$

$$\begin{aligned} &\text{Optimum level reached in previous cycles} \\ O^p &= (O^{s1}, O^{s2}, O^{s3}, \dots, O^{sn}), \end{aligned} \quad (7)$$

$$\text{Flying velocity } f^k = (f^{s1}, f^{s2}, f^{s3}, \dots, f^{sn}). \quad (8)$$

The final solution for all photos in each time is determined by the clearest picture (gbest) location (Pgbest). In order to reach as close to the best image gbest as possible, each image modifies its pace, and the updated velocities are provided here.

$$\begin{aligned} \text{New } f^k &= \gamma \times \text{present } f^k + M_1 \times \text{rand}(0, 1) \times (O^p - P^s) \\ &\quad + M_2 \times \text{rand}(0, 1) \times (O^p - P^s), \end{aligned} \quad (9)$$

where the two important constants referred to as training parameters are represented by  $M_1$  and  $M_2$ ; two randomized characteristics in the ranges  $(0, 1)$  are referred to as  $\text{rand}(0, 1)$ , and they have the possibility of causing a bigger shift in particles speed than  $P_{\max}$ ; and  $\gamma$  is the inertial mass, which is employed as a benefit to manage the impact of earlier acceleration at present speeds.

**4.6. Deep Learning.** The foundation of learning techniques is the creation of certain methods that enable computers to gain knowledge from experiences and resolve issues. When given data input and trained, a computational formula  $f$  can generate the required output. Rich data representation metadata is included in the training, which can provide the experience of deep-learning systems. An optimization technique then fine-tunes the algorithms that learned how to describe the data to generate specific estimates based on the discrepancy between both the currently anticipated outcome and the target outcome. The testing data, which are used to develop the model, provides feedback that is utilized to further fine-tune the model and assess its generalizability. The strategy is eventually tested on the testing sample after looping through these two processes to gauge how well it performs when presented with fresh, untested data. To determine whether the scientific formula  $f$  is capable of solving your assignment flawlessly, deep learning also requires the three processes of rating, fine-tuning, and assessment.

In accordance with the training phase, the information generally classifies deep learning into three groups. The first type is reinforcement learning, where the created agent interacts with its surroundings to maximize gains or find solutions to particular issues. Among its most well-known uses is Alpha Go, a Go-playing program created by neural net that even successfully defeated the best Go players around the world [26]. The unsupervised machine learning, which classifies or practices is implemented on training images with undetermined classes and identifies similarities among those,

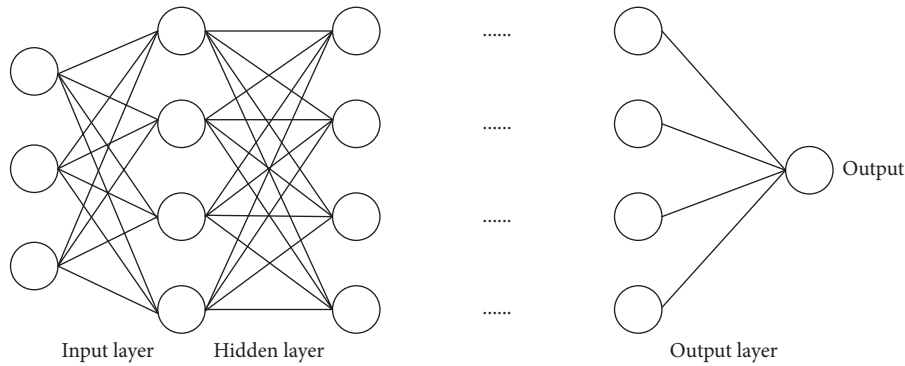


FIGURE 3: Schematic of CNN.

seems to be the second stage. Clustering is a well-known application of unsupervised classification. The final category is supervised learning, which is the focus of common machine learning algorithms because it requires matched datasets. Training on the labeled data to recognize patterns and their rules, and then generate the appropriate label on the omitted data. For instance, supervised learning is the foundation for several diagnostic imaging challenges, including PA image reconstruction [27]. Prior activation, traditional machine learning algorithms will directly or by employing the aid of many other straightforward deep learning algorithms collect characteristics from the data. While deep learning autonomously acquires interpretations and characteristics from the data as it goes through the training phase, deep learning would not necessitate human's architecture.

As an illustration, consider Figure 3's finest CNN, multilayer perceptron, or fully convolution layers network.  $C_k^l = \delta_k^{lT} y$ , wherein  $y$  is the quantity of the result of the prior level following the nonlinear function conversion known as the input signal, is the outcome of the  $i$ th-unit at layer  $j$ th. According to this after the input signal, the outcome of every layer is given to the following layer, where the exact computation is then carried out until the network generates the desirable result. The input layer receives the training data before performing the streaming computation and recording every network node outputs and derivatives. The error function then calculates the discrepancy between both the forecast and the labeling at the output nodes. The efficiency of the entire assignment is significantly impacted by the selection of gradient descent, so making that decision is important. Typical error function choices include mean average error and mean squared error. The loss function can also be created physically, which is frequently more appealing. To decrease mistakes, the weights of the system will be changed using the derivatives of the gradient descent as a feedback signal, which will travel backward through to the system. The network's composition will be modified to reduce mistakes using the derivatives of the gradient descent as a feedback controller, which will then travel backward throughout the system. The gradients of the objective function, especially compared to the parameters for each cluster, are determined using the inverse propagation technique, which uses the following expression.

Automated representations training, also serves as the primary distinction between contemporary deep-learning and traditional approaches to machine learning. The model improves both learning features and task performance simultaneously. With just an interactive book that uses the most widely used deep-learning approach in academics right now, PyTorch, anyone may explore deep learning in detail and gain a full understanding of it. In medical imaging, deep learning has advanced quickly, primarily using CNNs. Because CNNs can quickly pick up certain characteristics in images or other structured data, this really is advantageous. Next, we will briefly go through the fundamental elements of CNNs, so you can see why they are so effective and gain some insight into how to build your customized building.

**4.7. Structures of CNN.** The effectiveness of linking every cluster of all layers to all vertices of the following layer is relatively poor, despite the fact that the presented PSO can be actually applied to the visual. However, knowledge base may be used to reduce and connect structured data, such as photographs. CNNs are neural networks that, although having few connections, can maintain the spatial relationship between data. A CNN trains identically like an ANN, with the exception that it frequently has convolutional layers combined with kernel function and pooling layers. Figure 3 depicts CNN's workflow.

**4.7.1. Convolutional Layers.** The fully connected layer performs a combination process with a parameterized filter using the signals from the previous layer. This quantity of network variables can be significantly reduced by every filtering sharing value over the true extent, which also includes translational equivariance. A pooling layer is useful because properties displayed in one part of the image may also be displayed in other parts. For example, after training on weighting, this parametric filter can still identify the horizontal line at the bottom of the image in addition to the vertical axis. A tensor of extracted features would be produced following the convolution process of the fully connected layers.

**4.7.2. Activation Layers.** The initiation layer frequently consists of nonlinear authentication features. Nonlinear activation function ( $z$ ) =  $1/(1 + e - z)$  and rectification linearity units  $ReLU(z) = \max$  are examples of common convolution

layers ( $0, z$ ). There really are numerous additional categories of stimulation functions that can be chosen according to the mission and design. The neural network can nearly resemble any nonlinear function since it has those nonlinear activation functions and can combine them with linear operations like inversion. To discover more concerning the purpose of stimulation. Additionally, the activating layer produces fresh characteristic mapping transfer functions [28].

**4.7.3. Pooling.** The convolution layer produces a number for each small panel of the input nodes, which is commonly done using median or maximum pooling. Given that even a tiny change in the input would cause alterations in the feature map; the pooled gradient importance lies in providing the neural network with transcriptional nonlinearities. Translations and rotations, for instance, will not have an impact on the judgment outcome when determining whether the image contains red. The use of convolutional layers with longer strides as an alternative to pooling, which can simplify the network topology without degrading performance, has also been discovered in current studies. Increasing numbers of image recognition jobs are also favoring fully convolutional networks (FCNs) [29].

**4.7.4. Dropout.** The effectiveness of CNNs has been considerably enhanced by a fairly straightforward concept. To avoid CNNs from being overfitting, a dropout seems to be an aggregating method that employs probabilistic testing of cells. Every set of information employs an algorithm that is slightly different due to random neuron removal throughout training, as well as the parameters of the networks are adjusted based on the optimization of different networking variants.

**4.7.5. Batch Normalization.** By minimizing intrinsic covariate shift, batch normalization (BN) is a useful method for accelerating the learning of deep neural systems. Networks retraining is challenging because of the variable dispersion of network layer output outcomes resulting from changes in system parameters throughout training. By taking the mean from every training set and splitting it by the standard deviations, BN may create normalized feature maps. The training will be completed much more quickly because the data would be frequently altered to have a zero mean as well as a unit's standard error using BN. The original implementation and improvement of the CNN architecture will combine the abovementioned core components in a somewhat complex manner with a few novel and effective processes. When building your CNN, you frequently need to consider a lot of specifics in order for it to perform properly on a task. Users need to be thoroughly aware of the problem at hand before determining how to handle the statistical model and transmit it to the systems. The development of modules was frequently straightforward in the early stages of deep learning. However, when institutions became more and more complex, new, efficient architectural designs were created based on prior knowledge and observations, leading to improvements to the consist. Usually, such innovative structures are appropriate for acoustic imaging. Most of the papers that were looked into this can take some structural cues from these. However, signals domain 15 or

picture domain 16 may be processed separately to reduce noise or increase contrast before the information is inserted into the networks [30].

**4.8. Deep Learning for PAI.** Deep learning has been widely applied in clinics to aid physicians in providing more accurate diagnoses. This paper will only focus on deep learning in PA image analysis because there are so many deep-learning implementations in medical imagery across a variety of modalities. This is a tremendously rich, complex, and fascinating topic because effective examples usually involve many organs and have different technological and conceptual features [31]. Although PAT is a comparatively recent imaging method when compared to other health care diagnostic procedures, deep learning still offers a wide range of possible implications. Deep learning has particularly been used at each stage of the full PAI process. The mechanics of PA are relevant in order to generate elevated PA images from the sensor information. Relevant to the picture domain are illness separation, categorization, and diagnosis using the rebuilt PA images [32]. A special benefit of PAI over other imaging modalities is the provision of functional imaging capabilities without external contrast, include using imaging of oxygenation sufficiency.

**4.9. Reconstruction of Images.** After the process, ultrasonography imaging can be employed to reconstruct and categorize malignancy using the PS-CNN model. All inputs and outputs are viewed as independent of one another in the CNN. This presumption is untrue in many applications, particularly those that employ serial communication, like voice identification tools. In contrast to a typical neural network, CNN output is predicated on the prior level and occasionally serves a specific purpose for later elements. In other words, CNN-aided calculations from the past are stored in a recollection. CNNs are a type of neural network that are frequently employed for computational linguistics and have proven to be quite successful in tasks involving cancer diagnosis. The stream of data constantly travels from the layer of input to the layer, past the hidden layer. The data have indeed been transmitted through the network without passing over the identical nodes repeatedly, traveling straight from one node to another node. The CNN classification and its results are shown in Figure 4. Algorithm 1's technique for PS-CNN tumor reconstruction and recognition is described below.

This method suggested a deep learning-based optimization as the most popular method of optimization methodologies. Iteratively using PSO, the optimal overall solution, is possible. Figure 5 shows the PS-CNN approach's whole workflow.

## 5. Results and Discussion

**5.1. Experimentation and Learning.** The suggested network is trained, validated, and tested in the research using simulated tests. A variety of synthetic 2D target objects in different shapes and brightness make up each trial. The study selects



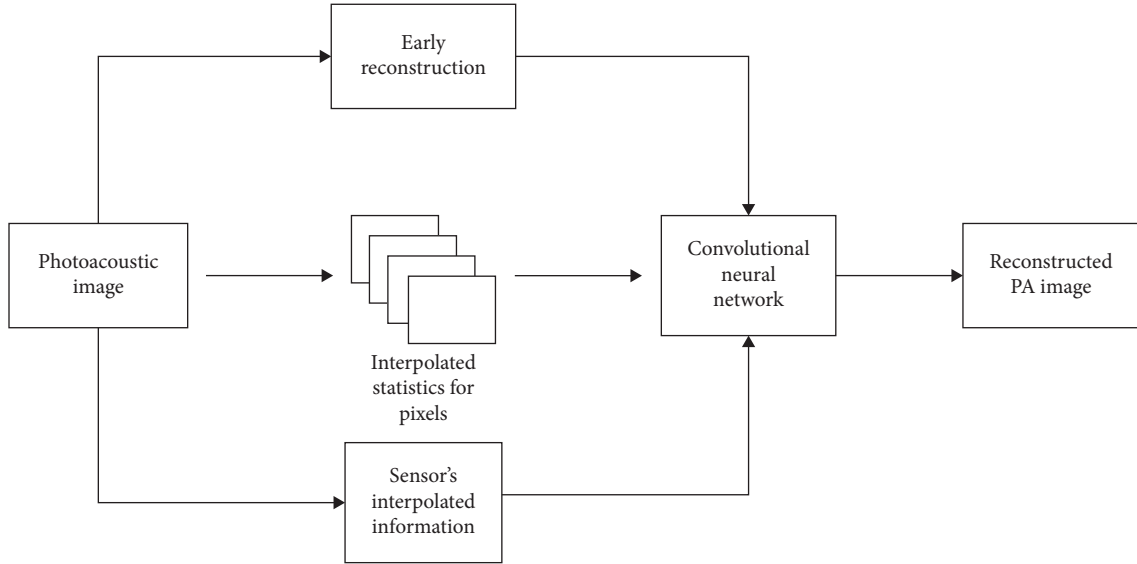
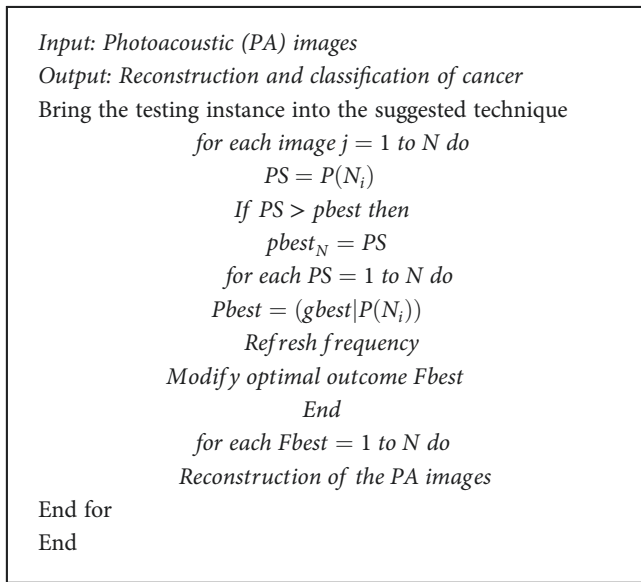


FIGURE 4: Workflow of CNN.



ALGORITHM 1: Proposed CNN-PS.

the entire amount of target entities (among one and six included) at randomly for every iteration. Additionally, the SoS of the backdrop and priorities is fixed for every test and is arbitrarily selected to fall between 1,500 and 1,650 m/s. Portable LED Net frameworks are used to represent every target, as well as the location of the target and its intensity values (which corresponds to contrasting) are both selected at random. To produce the projected visuals, the team ran a maximum of 7,000 iterations. Utilizing  $k$ -wave simulation toolkit, the study constructs the data of the system for every image while taking into account a linear actuator with 130 components at the top of the projected image (simulating PA action). In order to make the suggested system resilient against noise, the study has also included bilateral filtration of the channels information. Every test started with a

random selection of the noise variance, which is consistently smaller than the signal strength.

Everyone of the images is divided into three categories for the learning and validating sets in the research. For the learning, and validating sets, the distribution of the images is 70% and 30%, accordingly. As a result, there are 5,000 and 3,000 overall learning, and validating test images in this study, correspondingly.

**5.2. Validation and Learning Process.** The suggested network is trained in this research using the TensorFlow library and the PSO approach. With a minibatch size of 15, a cumulative of 7,000 epochs is utilized to improve the system parameters in the GPU. The learning phase rate is fixed at 85, and there is an exponentially decrease of the training set with a decay factor of 0.15 after every subsequent 3,000 eras. In this work, the validation data is used to adjust the higher parameters of the network, such as the size of convolutional kernel (99), the size of feature maps (16) in each dense transformation, the initial learning rate (103) in PSO, and the size of convolutional layers in each dense block (2). The training set is used to optimize the network parameters.

**5.3. Evaluation and Outcomes.** The study employs the peak signal-to-noise ratio (PSNR), which is dependent on the average squared loss among the predicted and referenced images in decibels (dB), to assess the suggested PS-CNN strategy using the validation set.

$$P_{SNR} = 20 \log_{10} \left( \frac{I_m}{\sqrt{mse}} \right), \quad (10)$$

$$mse = \frac{1}{XY} \sum_{x=0}^{X-1} \sum_{y=0}^{Y-1} (I_r(x, y) - I_e(x, y))^2, \quad (11)$$

where,  $I_m$  stands for the high intensities in the sample image, whereas  $I_r$  and  $I_e$  (both dimensions of  $X \times Y$ ) denote the

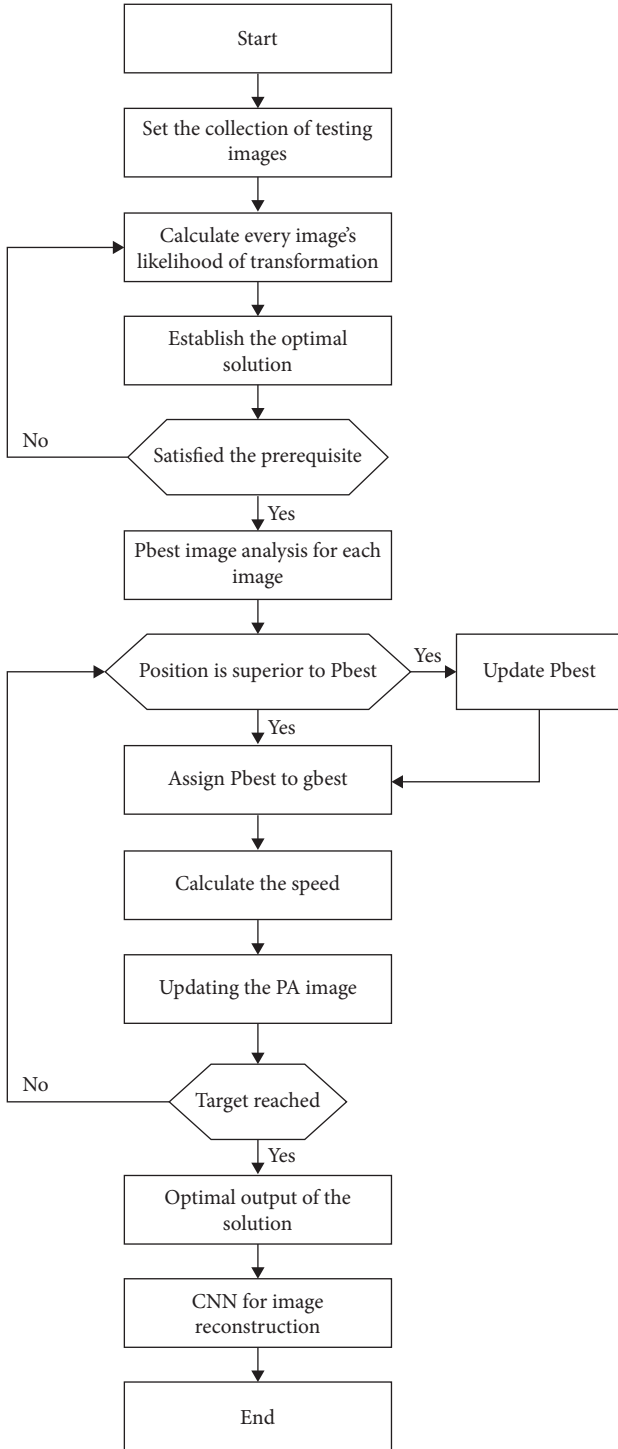


FIGURE 5: Proposed PS-CNN flowchart.

referenced and predicted images, correspondingly. The study looks into the suggested method’s sensitivity to SoS variability across many testing images in addition to the assessment based on PSNR. To do this, the study divides the whole SoS dispersal area (1,500–1,650 m/s) in the testing sample into 10 distinct nonoverlapping sets, after which the PSNR in the nonoverlapping zone is computed. The study also compares the suggested strategy with other traditional

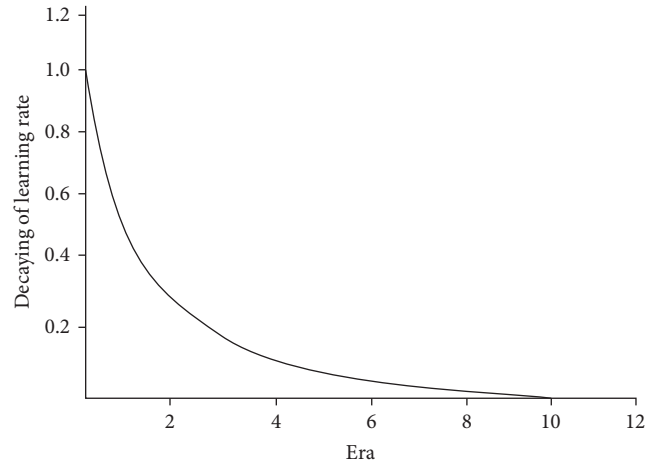


FIGURE 6: Decaying learned rate in terms of era.

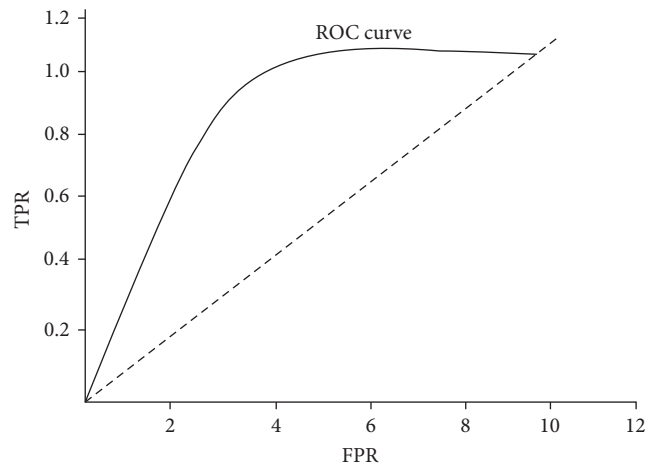


FIGURE 7: ROC curve based on true and FP rate.

techniques. It should be noted that in this analysis, the SoS value in the suggested technique is fixed at 1,600 m/s. To assess the suggested method’s real-time capacity, the study reports the calculation time on the GPU.

Research outperforms conventional techniques with a PSNR of  $39.5 \pm 5.6$  dB, based on 1,600 test sets. The pupil *t*-test’s *p*-value of 0.01 used to compare the empirical relevance of the findings from various tactics demonstrates how efficient the proposed approach works. During the learning phase, the variables of the CNN are changed via gradient descent. Figure 6 shows the collection of hyperparameters utilized in this scheme to choose the random beginning of the developed framework. These factors comprise the numbers of layers, thickness of the bilateral filter, fully linked layer, number of iterations, and transfer functions. Once the network has been trained, the training process is initially configured to run at a rate of 0.01 and the exponent of decay is roughly 0.1 for each era.

Figure 7 uses the training and validation database of MPA to show the ROC assessment of PS-CNN. It was

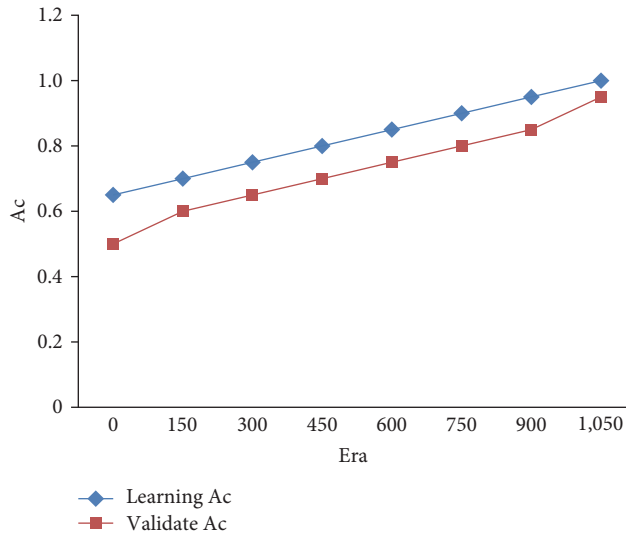


FIGURE 8: Learning and validating accurateness of PS-CNN approach.

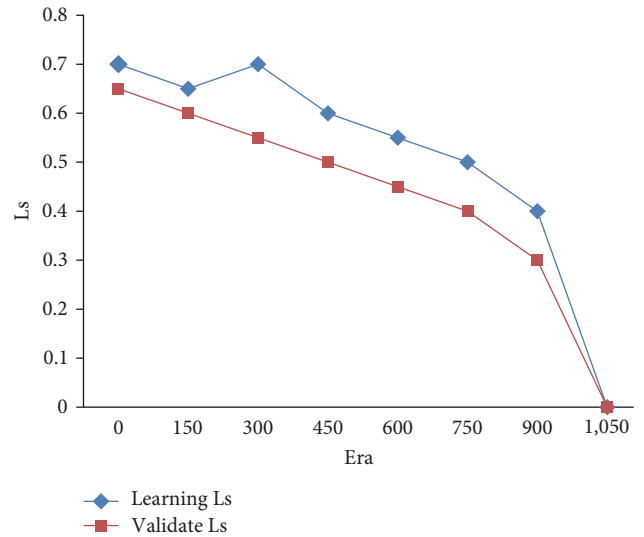


FIGURE 9: Learning and validating loss of PS-CNN approach.

TABLE 1: Compared the performance of the suggested method with other techniques.

Approach	PSNR	Ac	Pn	Rl	AUC measure	F1-measure
KNN	36.4 ± 4.5	92.5	91.5	90	90.4	91
SVM	38.2 ± 4.8	95.5	95.2	94.8	94.4	93
Naïve bayes	37.6 ± 4.4	89.8	89.5	89.2	88.4	88
RNN	35.2 ± 5.2	93.6	94	93.6	93.2	92.7
ANN	35.4 ± 4.2	98	97.2	94	94.5	93
Proposed PS-CNN	39.5 ± 5.4	99.5	99.0	96	98.5	95

Ac, abeats conventional techniques withcuracy; Pn, precision; PSNR, peak signal-to-noise ratio; Rl, recall.

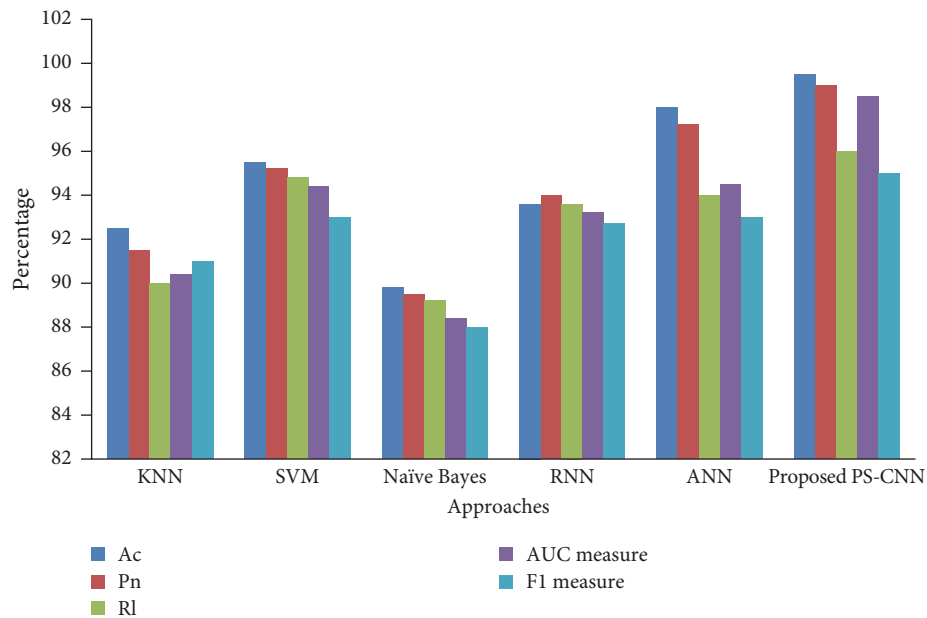


FIGURE 10: Comparisons of the suggested performance PS-CNN's with various established approaches.

revealed that on the training and validation sets, the suggested approach improved the area of the curve by roughly 99.5%. Figure 3 shows how accurately a dataset was trained and tested utilizing PS-CNN approach and how it turned out. When employing the suggested approach, the reliability of evaluating is improved in comparison to the efficiency of learning a dataset. The quantity of epochs determines how accurate the concentration value is.

Figures 8 and 9 show the damage caused by training and evaluating a set of data with the PS-CNN method using the MPA dataset. Depending on the percentage of eras, it is determined that the validating loss of the learning is minimized using this strategy, and the losing rate is saturation. The suggested approach's performance measurements are contrasted with those of existing approaches like the  $K$ -nearest neighbor, support vector mechanism, Naïve Bayes, recurrent neural network, and artificial neural network, which are displayed in Table 1 and shown graphically in Figure 10. Analysis shows that the suggested PS-CNN approach performs better than other strategies.

## 6. Conclusion

The study uses PA images to diagnose and categorize malignancy using a novel PS-CNN method. A unique PS-CNN-based technique was developed to enhance the quality of sparse PA images that may also speed up PAI. The collection of PA images of specimens was used to train the CNN technique. This technique's PSNR measurements are also utilized to demonstrate the suggested system's superior performance. The suggested PS-CNN technique includes CNN-based categorization, LED Net for separation depending on bilateral filtering processing, and PS-CNN for extracting features. The best possible outcomes of the PS-CNN strategy may be displayed via continuous simulations that make use of the benchmarking dataset. The PS-CNN approach fared better than any other option, according to comprehensive comparison studies. As a result, the PS-CNN model is a valuable tool for classifying cancer using PA images. The reliability of cancer categorization may be increased in the future using sophisticated DL methods.

## Data Availability

The data used to support the findings of this study are included within the article.

## Conflicts of Interest

The authors declare that they have no conflicts of interest.

## Acknowledgments

The authors would like to express their gratitude toward the Saveetha School of Engineering, SIMATS, Chennai, for providing the necessary infrastructure to carry out this work successfully.

## References

- [1] S.-W. Choe, H.-Y. Yoon, J.-Y. Jeong, J. Park, and J.-W. Jeong, "Automatic cancer cell taxonomy using an ensemble of deep neural networks," *Cancers*, vol. 14, no. 9, Article ID 2224, 2022.
- [2] R. A. Kruger, C. M. Kuzmiak, R. B. Lam, D. R. Reinecke, S. P. Del Rio, and D. Steed, "Dedicated 3D photoacoustic breast imaging," *Medical Physics*, vol. 40, no. 11, Article ID 113301, 2013.
- [3] L. Megalan Leo, A. Ranjith, and R. Thandaiah Prabu, "Analysis of mammogram images using active contour segmentation process and level set method," *International Journal of Emerging Technology and Advanced Engineering*, vol. 2, no. 2, 2012.
- [4] O. Vignesh, H. Mangalam, and S. Gayathri, "FPGA architecture for text extraction from images," *Cluster Computing*, vol. 22, pp. 12137–12146, 2019.
- [5] R. Sreelakshmy, A. Titus, N. Sasirekha et al., "An automated deep learning model for the cerebellum segmentation from fetal brain images," *BioMed Research International*, vol. 2022, Article ID 8342767, 13 pages, 2022.
- [6] A. Anbarasi, T. Ravi, V. S. Manjula et al., "A modified deep learning framework for arrhythmia disease analysis in medical imaging using electrocardiogram signal," *BioMed Research International*, vol. 2022, Article ID 5203401, 10 pages, 2022.
- [7] Z. Xie, F. M. Hooi, J. B. Fowlkes, R. W. Pinsky, X. Wang, and P. L. Carson, "Combined photoacoustic and acoustic imaging of human breast specimens in the mammographic geometry," *Ultrasound in Medicine and Biology*, vol. 39, no. 11, pp. 2176–2184, 2013.
- [8] G. Ramkumar, G. Anitha, M. Suresh Kumar, M. Ayyadurai, and C. Senthilkumar, "An effectual underwater image enhancement using deep learning algorithm," in *2021 5th International Conference on Intelligent Computing and Control Systems (ICICCS)*, pp. 1507–1511, IEEE, May 2021.
- [9] J. N. Swaminathan, S. Umamaheshwari, O. Vignesh et al., *Image Encryption Using Diffusion and Confusion Properties of Chaotic Algorithm*, Springer Singapore, Singapore, 2022.
- [10] H. Shahid, A. Khalid, Y. Yue, X. Liu, and D. Ta, "Feasibility of a generative adversarial network for artifact removal in experimental photoacoustic imaging," *Ultrasound in Medicine and Biology*, vol. 48, no. 8, pp. 1628–1643, 2022.
- [11] Y. Qi, H. Cao, G. Yin, B. Zhang, and J. Guo, "Optimized reconstruction procedure of photoacoustic imaging for reflection artifacts reduction," *Ultrasonic Imaging*, vol. 44, no. 5-6, pp. 204–212, 2022.
- [12] Y. Wang, C. Yuan, J. Jiang, K. Peng, and B. Wang, "Photoacoustic/ultrasound endoscopic imaging reconstruction algorithm based on the approximate gaussian acoustic field," *Biosensors*, vol. 12, no. 7, Article ID 463, 2022.
- [13] M. Shi, T. Zhao, S. J. West, A. E. Desjardins, T. Vercauteren, and W. Xia, "Improving needle visibility in LED-based photoacoustic imaging using deep learning with semi-synthetic datasets," *Photoacoustics*, vol. 26, Article ID 100351, 2022.
- [14] I. Steinberg, J. Kim, M. K. Schneider et al., "Superiorized Photo-Acoustic Non-NEgative Reconstruction (SPANNER) for clinical photoacoustic imaging," *IEEE Transactions on Medical Imaging*, vol. 40, no. 7, pp. 1888–1897, 2021.
- [15] A. P. Rao and S. Sinha, "Performance comparison of acoustic lens based photoacoustic image reconstruction with algorithm based reconstruction techniques," *Optik*, vol. 243, Article ID 167512, 2021.
- [16] S. Agrawal, T. Suresh, A. Garikipati, A. Dangi, and S.-R. Kothapalli, "Modeling combined ultrasound and photoacoustic imaging:



- simulations aiding device development and artificial intelligence,” *Photoacoustics*, vol. 24, Article ID 100304, 2021.
- [17] H. Jin, Z. Zheng, S. Liu et al., “Pre-migration: a general extension for photoacoustic imaging reconstruction,” *IEEE Transactions on Computational Imaging*, vol. 6, pp. 1097–1105, 2020.
- [18] H. Jin, S. Liu, R. Zhang, S. Liu, and Y. Zheng, “Frequency domain based virtual detector for heterogeneous media in photoacoustic imaging,” *IEEE Transactions on Computational Imaging*, vol. 6, pp. 569–578, 2020.
- [19] E. Najafzadeh, P. Farnia, S. N. Lavasani et al., “Photoacoustic image improvement based on a combination of sparse coding and filtering,” *Journal of Biomedical Optics*, vol. 25, no. 10, Article ID 106001, 2020.
- [20] L. V. Wang and J. Yao, “A practical guide to photoacoustic tomography in the life sciences,” *Nature Methods*, vol. 13, pp. 627–638, 2016.
- [21] S. Hu, K. Maslov, and L. V. Wang, “Second-generation optical-resolution photoacoustic microscopy with improved sensitivity and speed,” *Optics Letters*, vol. 36, no. 7, pp. 1134–1136, 2011.
- [22] C. P. Favazza, L. V. Wang, and L. A. Cornelius, “*In vivo* functional photoacoustic microscopy of cutaneous microvasculature in human skin,” *Journal of Biomedical Optics*, vol. 16, no. 2, Article ID 026004, 2011.
- [23] B. E. Treeby, E. Z. Zhang, and B. T. Cox, “Photoacoustic tomography in absorbing acoustic media using time reversal,” *Inverse Problems*, vol. 26, no. 11, Article ID 115003, 2010.
- [24] R. Manwar, M. Zafar, and Q. Xu, “Signal and image processing in biomedical photoacoustic imaging: a review,” *Optics*, vol. 2, no. 1, pp. 1–24, 2021.
- [25] Y. Wang, Q. Zhou, J. Liu et al., “LEDNet: a lightweight encoder-decoder network for real-time semantic segmentation,” 2019.
- [26] D. Silver, J. Schrittwieser, K. Simonyan et al., “Mastering the game of go without human knowledge,” *Nature*, vol. 550, pp. 354–359, 2017.
- [27] A. Hauptmann, F. Lucka, M. Betcke et al., “Model-based learning for accelerated, limited-view 3-D photoacoustic tomography,” *IEEE Transactions on Medical Imaging*, vol. 37, no. 6, pp. 1382–1393, 2018.
- [28] K. He, X. Zhang, S. Ren, and J. Sun, “Delving deep into rectifiers: surpassing human-level performance on ImageNet classification,” in *2015 IEEE International Conference on Computer Vision (ICCV)*, pp. 1026–1034, IEEE, Santiago, Chile, December 2015.
- [29] J. Long, E. Shelhamer, and T. Darrell, “Fully convolutional networks for semantic segmentation,” in *2015 IEEE Conference on Computer Vision and Pattern Recognition (CVPR)*, pp. 3431–3440, IEEE, Boston, MA, USA, June 2015.
- [30] A. Khan, A. Sohail, U. Zahoora, and A. S. Qureshi, “A survey of the recent architectures of deep convolutional neural networks,” *Artificial Intelligence Review*, vol. 53, pp. 5455–5516, 2020.
- [31] A. S. Lundervold and A. Lundervold, “An overview of deep learning in medical imaging focusing on MRI,” *Zeitschrift für Medizinische Physik*, vol. 29, no. 2, pp. 102–127, 2019.
- [32] Y. E. Boink, S. Manohar, and C. Brune, “A partially-learned algorithm for joint photo-acoustic reconstruction and segmentation,” *IEEE Transactions on Medical Imaging*, vol. 39, no. 1, pp. 129–139, 2020.